S23. INVESTIGATING THE INFLUENCE OF ANTHROPOGENIC FORCING AND NATURAL VARIABLLILITY ON THE 2014 HAWAIIAN HURRICANE SEASON

H. Murakami, G. A. Vecchi, T. L. Delworth, K. Paffendorf, R. Gudgel, L. Jia, and F. Zeng

Model description

We used the Geophysical Fluid Dynamics Laboratory (GFDL) Forecast-oriented Low Ocean Resolution model (FLOR; Vecchi et al. 2014). FLOR comprises 50-km mesh atmosphere and land components and 100-km mesh sea ice and ocean components. The atmosphere and land components of FLOR are taken from the Coupled Model version 2.5 (CM2.5; Delworth et al. 2012) developed at GFDL, whereas the ocean and sea ice components are based on the GFDL Coupled Model version 2.1 (CM2.1; Delworth et al. 2006; Wittenberg et al. 2006; Gnanadesikan et al. 2006).

A suite of simulations (see the following section for experimental design) were conducted using the "flux adjustments" approach (Magnusson et al. 2013; Vecchi et al. 2014), which adjusts the model's momentum, enthalpy, and freshwater fluxes from atmosphere to ocean and so brings the long-term climatology of sea surface temperature (SST) and surface wind stress closer to the observations.

Detection algorithm for tropical cyclones

Model generated tropical cyclones (TCs) were detected following Murakami et al. (2015), and the description below is taken from Section 2c in Murakami et al. (2015).

Model-generated TCs were detected directly from 6-hourly output using the following tracking scheme relying primarily on sea level pressure (SLP) and temperature anomaly (t_a) averaged between 300 and 500 hPa.

1. Local minima in a smoothed SLP field are detected. The location of the center is fine-tuned by fitting a biquadratic to the SLP field and placing the center at its minimum.
2. Closed contours of some specified interval dp (here 2 hPa) are found about each center. The *Nth* contour is identified as the contiguous region surrounding a low of central pressure P, with pressures less than $dp \times N + P$, as found by a "flood fill" algorithm. Hence, the contours need not be circular; however, there is a maximum distance of 3000 km that the algorithm will search away from the candidate low center.
3. If the above closed contours are found, the low is counted as a storm center at that time. The tracker then tries to find as many closed contours about that low that it can find without going too far from the low center or running into contours claimed by another low. The maximum 10-m wind inside the set of closed contours is considered to be the maximum wind speed for the storm at that time.
4. Warm cores are found through a similar process as above: closed 1-K contours about the maximum t_a are sought out within a storm's identified contours, which are not more than 1° apart from the low center. This contour must have a radius less than 3° in distance. If no such core is found, the center is not

rejected, but is simply marked as not being a warm-core low.

5. Storm centers are connected into a track by taking a low center at time $T - dt$, extrapolating its motion forward dt, and then looking for storms within 750 km. Deeper lows get first choice of track.

6. Final TCs are selected by considering satisfactions of duration conditions as follows.

(i) At least 72 hours of total detection lifetime.

(ii) At least 48 cumulative (not necessarily consecutive) hours of having a warm core.

(iii) At least 36 consecutive hours of a warm core plus winds greater than 15.5 m s^{-1}.

(iv) The start (last) time of 24 consecutive hours of a warm core plus winds is assigned to genesis (cyclolysis) time. Location of TC genesis should be equatorward of 40°N.

TC positions are counted for each $2.5° \times 2.5°$ grid box within the global domain at 6-hour intervals. The total count for each grid box is defined as the TC density. The density fields are smoothed using a 9-point moving average weighted by distance from the center of the grid box. TC density is used in the following regression analysis (see Supplemental Figs. S23.2–S23.5).

Experimental settings

We conducted a suite of simulations using FLOR. A large number of samples are required to compute the probability of occurrence of a year with TC frequency more than or equal to a specific number [$P(x)$]. A detailed description of how we calculated the probability for each simulation is given below.

Retrospective seasonal forecasts. For each year in the period 1980–2014, we used the results of 12-member ensemble retrospective seasonal forecasts by FLOR (Vecchi et al. 2014; Jia et al. 2015). For each ensemble member, 12-month duration predictions were performed after initializing the model to observationally constrained conditions. The 12-member initial conditions for ocean and sea ice components were built through a coupled ensemble Kalman filter (EnKF) data assimilation system developed for CM2.1, whereas those for atmosphere

and land components were built from a suite of SST-forced atmosphere–land-only simulations using the components in FLOR. Therefore, the predictability in these experiments comes entirely from the ocean and sea ice, and may be thought of as a lower bound on the potential prediction skill of a model, because predictability could also arise from atmospheric (particularly stratospheric) and land initialization.

We used 12-member ensemble forecasts initialized on 1 July to evaluate model skill in predicting TC frequency near Hawaii during the subsequent TC season (July–November).

1860/1990-control simulations. We generated 2000-year control climate simulations using FLOR by prescribing radiative forcing and land-use conditions representative of the year 1860. In addition, we generated 500-year control climate simulations by prescribing conditions representative of the year 1990. For these experiments, we compute $P(x)$ using all simulated years. Results are shown in Fig. 23.2b in the main text. To elucidate multicentury variability, we compute $P(x)$ for each 100-year period. The error bars in Fig. 23.2b show the range of minimum and maximum in the variability.

Multidecadal simulations. We conducted 35-member ensemble multidecadal simulations using FLOR (Supplemental Fig. S23.1). Five- (thirty-) member ensemble simulations were conducted from 1861
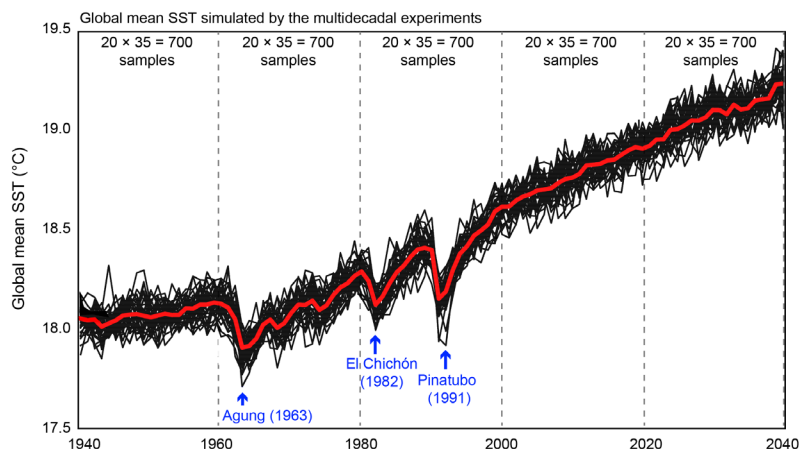
Fig S23.1 Interannual variation of global mean SST (°C) simulated by the multidecadal experiment from the period 1941–2040. Black line shows simulated global mean SST for each ensemble member. Red line shows ensemble mean value. Blue arrows denote historical volcanic events. The simulated internal variability is out of phase among the ensemble members, whereas the ensemble mean shows a significant positive trend due to the response of anthropogenic forcing along with a few abrupt decreases due to volcanic forcing. For each 20-year period, 700 (20 years × 35 ensemble members) samples are obtained to compute $P(x)$.

(1941) to 2040 by prescribing historical anthropogenic forcing and aerosols up to 2005, and future levels based on the RCP4.5 scenario from 2006 to 2040. In the simulations, historical volcanic radiative forcing was also prescribed up to 2005; however, no volcanic forcing was prescribed after 2006. These multidecadal simulations were not initialized experiments, that is, simulated internal variability, such as ENSO, was out of phase among the ensemble members and observations. For each 20-year period from 1941, 700 (= 20 × 35) samples were available to calculate $P(x)$.

Indices for natural variability

To elucidate the potential influence of natural variability on the frequency of TCs near Hawaii, we focused on the El Niño–Southern Oscillation (ENSO), Pacific decadal oscillation (PDO; Mantua et al. 1997), interdecadal Pacific oscillation (IPO; Power et al. 1999; Folland et al. 2002), and Atlantic multidecadal oscillation (AMO; Delworth and Mann 2000). We focused on these indices during the boreal summer of July–November to compare them with TC frequency near Hawaii. In this section, we describe how to calculate those climate indices. Note that we focused mainly on decadal time scales for PDO, IPO, and AMO, whereas we focused on interannual time scales for ENSO.

ENSO (Niño-3.4 index). We used Niño-3.4 index to represent ENSO. The Niño-3.4 index is obtained from the mean SST anomaly in the region bounded by 5°N and 5°S, and between 170°W to 120°W. The SST anomaly is calculated by subtracting the climatological mean value. For the 1860- (1990-) control simulation, we used the 2000-yr (500-yr) mean for the climatological mean. For the multidecadal simulations, we defined the climatological mean value for each year using a 21-yr moving average to smooth the nonlinear trend of global warming. The Niño-3.4 index is standardized after calculating the anomaly (i.e., its mean value is zero and its standard deviation is one). We defined a positive phase of ENSO (i.e., El Niño) as years in which the Niño-3.4 index exceeds one standard deviation.

Likewise, we defined a negative phase of ENSO (i.e., La Niña) years in which the Niño-3.4 index falls below minus one standard deviation.

Supplemental Fig. S23.2 shows the observed Niño-3.4 index as well as the regression of SST and TC density onto the Niño-3.4 index. When the Niño-3.4 index is positive (i.e., an El Niño year), the tropical eastern Pacific is warmer than normal. Moreover, TC density increases in the eastern Pacific when the Niño-3.4 index is positive, leading to an increased TC frequency near Hawaii. The Niño-3.4 index during the 2014 TC season was 0.5.

Pacific decadal oscillation (PDO index). We calculated the PDO index following Mantua et al. (1997). The PDO is the leading empirical orthogonal function (EOF) of SST anomalies over the North Pacific
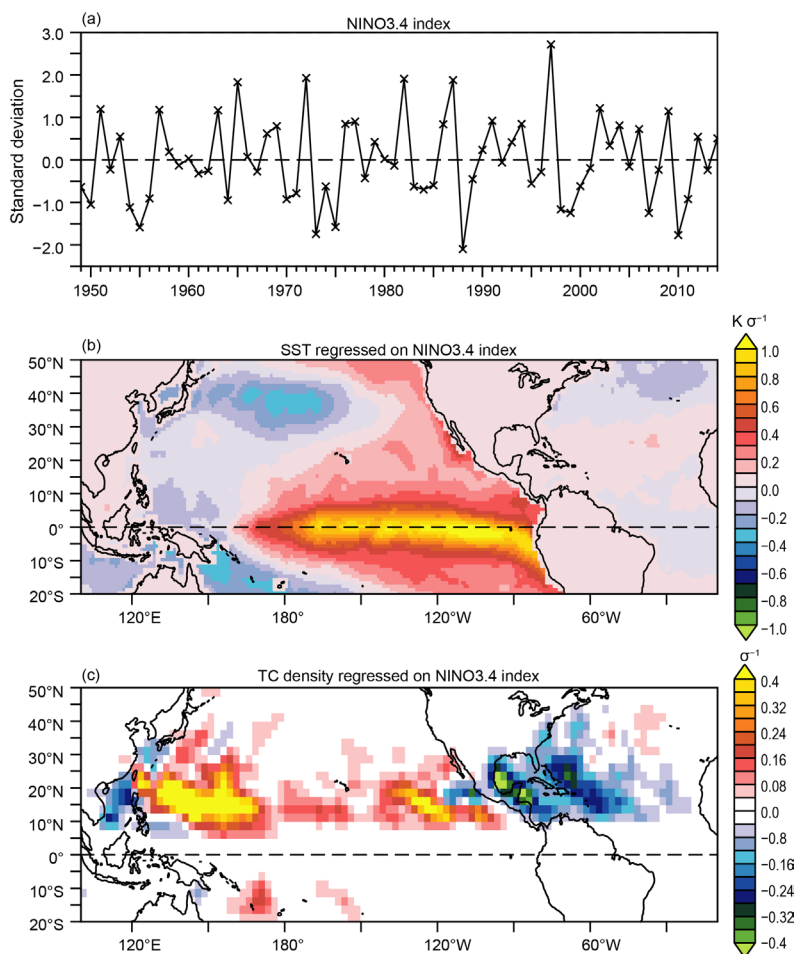
FIG. S23.2. Observed mean Niño-3.4 index for July–November (1949–2014). (a) Time series of Niño-3.4 index for the period 1949–2014 [units: 1σ (one standard deviation)]. (b) Seasonal mean SST regressed onto the Niño-3.4 index (units: K σ⁻¹). (c) Seasonal mean TC density regressed onto the Niño-3.4 index (units: number σ⁻¹). The HadISST1.1 was used for SST, whereas the IBTrACS plus Unisys best-track data were used for TC density.

(20°–70°N, 110°E–100°W) after the global mean SST has been removed. The PDO index is the standardized principal component time series. To focus on the decadal variation of the PDO, we used a 10-yr low-pass filtered index throughout this study. We defined a positive (negative) phase of the PDO as years in which the filtered PDO index falls below one (minus one) standard deviation.

Supplemental Fig. S23.3 shows the observed PDO index as well as the regression of SST and TC density onto the PDO index. When the PDO index is positive, the subtropical eastern Pacific (north Pacific) is warmer (cooler) than normal. Moreover, TC density increases in the eastern Pacific when the PDO index is positive, leading to an increase in TC frequency near Hawaii. The PDO index during the 2014 TC season was −0.7.

Interdecadal Pacific oscillation (IPO index). We calculated the IPO index following Folland et al. (1999, 2002) and Power et al. (1999). The IPO index is the standardized 3rd principal component of the EOF for the 13-yr low-pass filtered global SST. The IPO

manifests as a low-frequency El Niño-like pattern of climate variability, whose spatial pattern is similar to that of the global warming hiatus seen in recent decades as (England et al. 2014). We defined a positive (negative) phase of the IPO as years in which the IPO index falls below one (minus one) standard deviation.

Supplemental Fig. S23.4 shows the observed IPO index as well as the regression of SST and TC density onto the IPO index. When the IPO index is positive, the subtropical eastern Pacific (north Pacific) is warmer (cooler) than normal, which is similar to the PDO (Supplemental Fig. S23.3). Moreover, TC density increases in the eastern Pacific when the IPO index is positive, leading to an increase in TC frequency near Hawaii. The IPO index during the 2014 TC season was −2.0.

Atlantic multidecadal oscillation (AMO index). We calculated the AMO index following Deser et al. (2010). The AMO index is defined as the area-average SST anomaly over the North Atlantic (0°–70°N, 90°W–0°) minus the global mean SST anomaly. The AMO index was standardized after calculating the anomalies.

To focus on the decadal variation of the AMO, we used a 10-yr low-pass filtered index throughout this study. We defined a positive (negative) phase of the AMO as years in which the AMO index falls below one (minus one) standard deviation.

Supplemental Fig. S23.5 shows the observed AMO index as well as the regression of SST and TC density onto the AMO index. When the AMO index is positive, the North Atlantic is warmer than normal. Unlike other indices, TC density decreases in the eastern Pacific when the AMO index is positive, indicating that TC frequency near Hawaii should increase when the AMO index is negative. The AMO index during the 2014 TC season was +0.7.
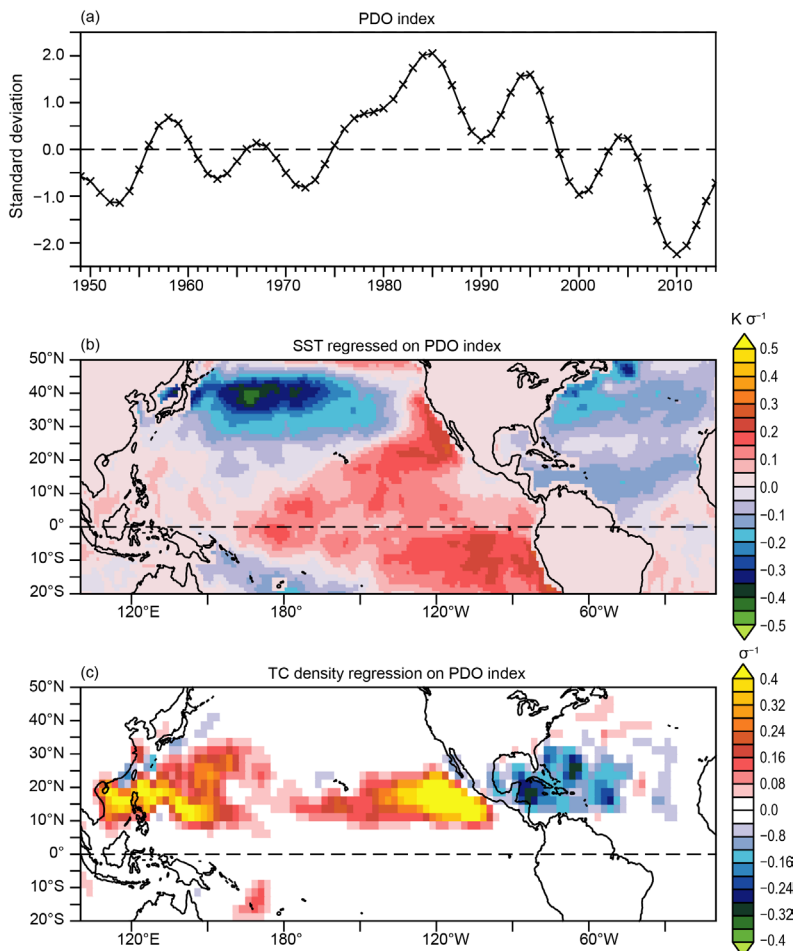
FIG. S23.3. As in Fig. S23.2, but for the PDO index.
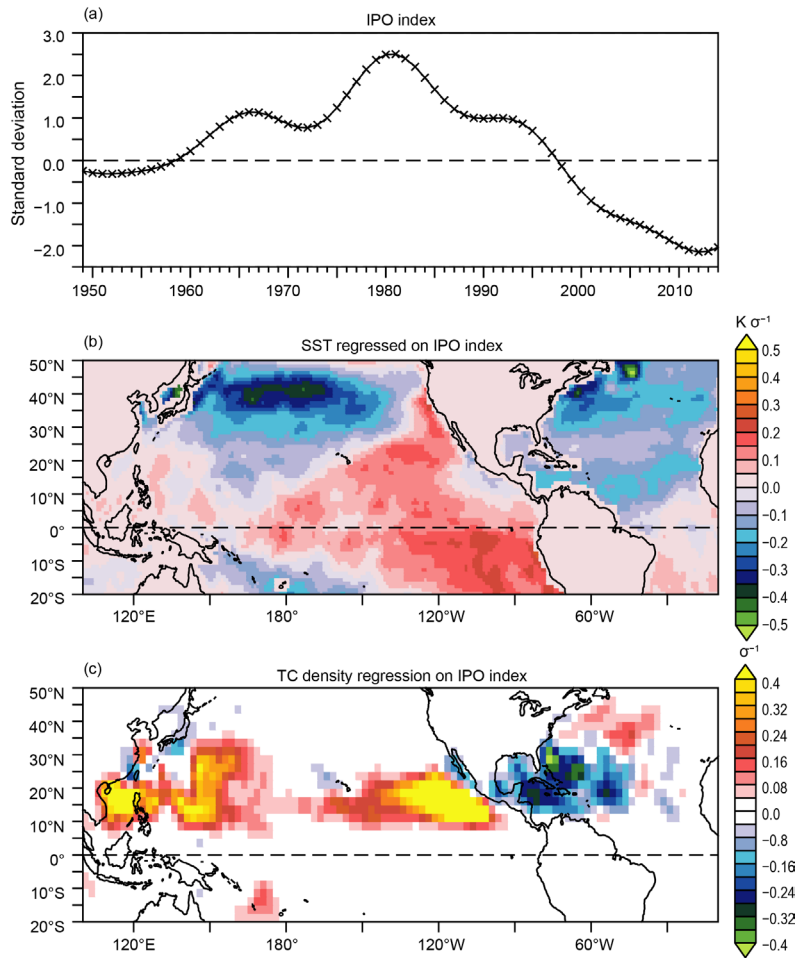
Fɪɢ. S23.4. As in Fig. S23.2, but for the IPO index.
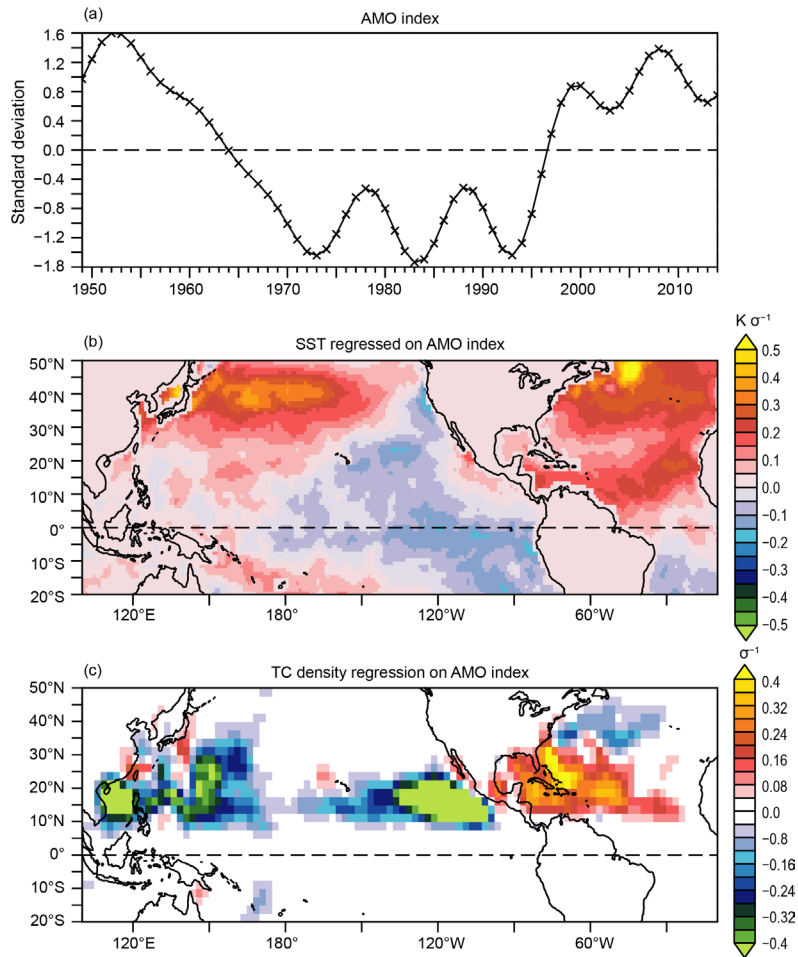
FIG. S23.5. As in Fig. S23.2, but for the **AMO index**.

REFERENCES

Delworth, T. L., and M. E. Mann, 2000: Observed and simulated multidecadal variability in the Northern Hemisphere. *Climate Dyn.*, **16**, 661–676.

——, and Coauthors, 2006: GFDL's CM2 global coupled climate models. Part I: Formulation and simulation characteristics. *J. Climate*, **19**, 643–674.

——, and Coauthors, 2012: Simulated climate and climate change in the GFDL CM2.5 high-resolution coupled climate model. *J. Climate*, **25**, 2755–2781, doi:10.1175/JCLI-D-11-00316.1.

Deser, C., M. A. Alexander, S.-P. Xie, and A. S. Phillips, 2010: Sea surface temperature variability: Patterns and mechanisms. *Annu. Rev. Mar. Sci.*, **2**, 115–143.

England, M. H., and Coauthors, 2014: Recent intensification of wind-driven circulation in the Pacific and the ongoing warming hiatus. *Nat. Climate Change*, **4**, 222–227, doi:10.1038/nclimate2106.

Folland, C. K., D. E. Parker, A. Colman, and R. Washington, 1999: Large scale modes of ocean surface temperature since the late nineteenth century. *Beyond El Nino: Decadal and Interdecadal Climate Variability*, A. Navarra, Ed., Springer, 73–102.

——, J. A. Renwick, M. J. Salinger, and A. B. Mullan, 2002: Relative influences of the Interdecadal Pacific Oscillation and ENSO on the South Pacific Convergence Zone. *Geophys. Res. Lett.*, **29** (13), doi:10.1029/2001GL014201.

Gnanadesikan, A., and Coauthors, 2006: GFDL's CM2 global coupled climate models. Part II: The baseline ocean simulation. *J. Climate*, **19**, 675–697.

Jia, L., and Coauthors, 2015: Improved seasonal prediction of temperature and precipitation over land in a high-resolution GFDL climate model. *J. Climate*, **28**, 2044–2062, doi:10.1175/JCLI-D-14-00112.1.

Magnusson, L., M. Alonso-Balmaseda, S. Corti, F. Molteni, and T. Stockdale, 2013: Evaluation of forecast strategies for seasonal and decadal forecasts in presence of systematic model errors. *Climate Dyn.*, **41**, 2393–2409, doi:10.1007/s00382-012-1599-2.

Mantua, N. J., S. R. Hare, Y. Zhang, J. M. Wallace, and R. C. Francis, 1997: A Pacific interdecadal climate oscillation with impacts on salmon production. *Bull. Amer. Meteor. Soc.*, **78**, 1069–1079.

Murakami, H., and Coauthors, 2015: Simulation and prediction of category 4 and 5 hurricanes in the high-resolution GFDL HiFLOR coupled climate model. *J. Climate*, in press, doi:10.1175/JCLI-D-15-0216.1.

Power, S., T. Casey, C. Folland, A. Colman, and V. Mehta, 1999: Interdecadal modulation of the impact of ENSO on Australia. *Climate Dyn.*, **15**, 319–324.

Vecchi, G. A., and Coauthors, 2014: On the seasonal forecasting of regional tropical cyclone activity. *J. Climate*, **27**, 7994–8016, doi:10.1175/JCLI-D-14-00158.1.

Wittenberg, A. T., A. Rosati, N.–C. Lau, and J. J. Ploshay, 2006: GFDL's CM2 global coupled climate models. Part III: Tropical pacific climate and ENSO. *J. Climate*, **19**, 698–722.